2013-11

Least-squares phase estimation with wrapped measurements and branch points

Cristi, Roberto

Least-squares phase estimation with wrapped measurements and branch points

Roberto Cristi* and Travis W. Axtell

Department of Electrical and Computer Engineering, Naval Postgraduate School Spanagel Hall, Room 437, 833 Dyer Road, Monterey, California 93943-5216, USA
**Corresponding author: rcristi@nps.edu*

Received May 1, 2013; revised September 6, 2013; accepted September 8, 2013; posted September 9, 2013 (Doc. ID 189823); published October 7, 2013

A nonorthogonal model for 2D signals with rotational components is presented, which enables estimation of phase values from observations of its local gradients. In this research, the rotational components are caused by the presence of branch points, which indicates phase wrapping. Using the proposed model, the phase is estimated using standard least-squares or recently proposed wavelet techniques by processing a linear combination of the wrapped observed gradients and the curl generated by phase wrapping.

OCIS codes: (010.7350) Wave-front sensing; (010.1330) Atmospheric turbulence; (010.7060) Turbulence; (100.5088) Phase unwrapping; (280.6730) Synthetic aperture radar.
http://dx.doi.org/10.1364/JOSAA.30.002225

1. INTRODUCTION

The problem of estimating the phase of a two- or three-dimensional signal from local gradients is at the basis of numerous applications in advanced imaging. Typical examples are applications in adaptive optics, where the goal is to estimate phase distortion due to atmosphere, and interferometric synthetic aperture radar, where high-resolution images are constructed from local phase differences from a coherent source.

Although the problem in itself has an abundance of data, since in the 2D case for every phase value to reconstruct there are two gradient values we observe, the fact that the phase is ambiguously measured with multiples of 2π rad makes the problem particularly challenging, at least in certain applications.

The phase function of a wavefront is defined in a 2D plane that provides information on the electric field entering an optical system pupil. Ideally this function would be a constant across the aperture for all time. However, since the atmosphere has mixing, adaptive optics were developed to correct for the distortion. Adaptive optics systems for science telescopes are designed for light-to-moderate turbulence at good-seeing telescope facilities. These systems rely on sensors that make gradient measurements of the field and reconstruct the wavefront to provide an appropriate control law to command a deformable mirror. However, for systems that require long, horizontal paths through the atmosphere, the cumulative turbulence can create branch points in the phase function, which are located in areas of low amplitude intensity of the electric field. Branch points were first observed by Nye and Berry in 1974 [1].

Not all measured gradient fields ("slopes" in adaptive optics) form continuous, smooth wavefront surfaces. Said another way, not all vector fields are gradients of functions. This is the difficulty with branch points in reconstruction: the reconstructed surface can no longer be smooth and some areas of the reconstructed surface will have discontinuities. However, a least-squares reconstructor cannot produce these discontinuities, and incorrectly estimates the phase values across the wavefront surface. Although a smooth phase function cannot be determined, there is a family or ensemble of phase functions that all have the same gradient measurements and different algorithms may result in different phase functions using the same measurements for this reason. Unwrapped phase functions are also members of the ensemble.

The original work in reconstruction when branch points are present was done by Fried and Vaughn [2]. The paper provided analysis that branch points appear in areas of low intensity. The wavefront reconstruction used a branch cut reconstructor, which places branch cuts to prevent path-dependent phase unwrapping from traversing the cuts. The branch cuts were placed in areas of low intensity by taking irradiance (SNR) into account, which improves the adaptive optics system performance.

A few years later, Fried [3] and Tyler [4] continued the analysis work of branch points in wavefront reconstruction. In both works, the observed gradient phase field is decomposed into irrotational and rotational components, associated to a scalar (irrotational) and a vector (rotational) potentials. Both components are orthogonal to each other and the rotational component is hidden in the null space of the standard least-squares reconstructor.

In [3], Fried uses the continuous-variable locations of branch points to calculate the hidden component of the phase. The principal-value gradient measurements are restricted to $[-\pi, \pi)$ and result in a "hidden phase" that is hidden to the least-squares wavefront reconstruction algorithms. He locates branch points using a derivation based on the curl of the vector potential. After determining branch point locations, the hidden phase can be determined and summed with the output of the least-squares solution to determine the total phase. His follow-on work included a complex exponential reconstructor

that solves for the phase using phasors and the Smooth Phase algorithm to place branch cuts along low-intensity paths [5].

In [4], Tyler uses a Fourier space formulation to describe how the two orthogonal components depend on the gradient field. The "slope discrepancy" was determined to be the difference of the gradient field of the reconstructed surface and the original measurements. He defines the slope discrepancy as a matrix operator on the gradient measurements that can be used to reconstruct the correction to the least-squares wavefront reconstruction. The correction presented by Tyler procedurally follows the least-squares reconstructor, whereas ours presented here is performed before the reconstructor.

After determining the phase values, the phase must still be unwrapped. One technique to accomplish this in the presence of branch points is a path-dependent solution using branch cuts. These cuts are placed between branch points of opposite sign (polarity) and prevent any unwrapping path through the cut. This problem was also discussed in the synthetic aperture radar interferometry community [6]. A significant issue with this approach deals with the possibility that branch cuts may disconnect areas of the data and may not unwrap properly. Numerous algorithms have been developed to unwrap and mitigate this issue [2,7–10]. In the radar community, processing speed is not as critical to system operation as in adaptive optics. For this reason, additional techniques have been sought to improve calculation performance. In our work presented here, we do not perform phase unwrapping and leave that as a follow-on procedure after a phase function member of the ensemble is determined.

Wavefront sensors for adaptive optics have been studied to determine their performance in strong scintillation, which indicates branch points are present. The Shack–Hartmann sensor degrades from random apodization in the subapertures as the Rytov number increases [11], and a shearing or point diffraction interferometer may be a better choice [12]. The algorithm presented in this paper does not cover the effects of scintillation on the physics of the wavefront sensor; however, the algorithm presented here does cover the effects of branch points on the reconstruction algorithm.

Detection of branch point locations has been accomplished by a variety of methods. Fried and Vaughn started the contour sum technique [2]. The branch point potential method was first proposed by Le Bigot and Wild [13]. Murphy *et al.* have been evaluating branch point sensitive reconstructors in closed-loop experiments [14]. Zetterlind and Magee evaluated the performance of branch point tolerant reconstructors with time delays [15].

Research is also being conducted into the fundamental nature of branch points. Atmospheric branch points have been shown to create in pairs and evolve smoothly in time [16]. The gradient measurements have been used to estimate the turbulence layers' altitude and strength [17–20]. Sanchez and Oesch have proposed that branch points indicate the presence of photons with nonzero orbital angular momentum [21,22].

In this paper, we derive the relationship of the phase and vector potential to the gradient measurements using a nonorthogonal basis for both continuous and discrete signals. This approach allows for solving for the atmospheric-induced branch point locations. Using this approach, a least-squares solution is possible which directly accounts for the hidden phase from the branch points. The ambiguous multiples of 2π phase are solved directly. The phase still requires to be unwrapped. Simulations are shown to verify performance for data with square aperture support.

This paper is organized as follows: in Section 2, we provide the notation and preliminary mathematics used in this paper. In Section 3, the vector field decomposition is explained. Section 4 is the description and comparison of Fried gradients and wrapped Fried gradients. Section 5 is the main result of this paper and has the least-squares phase estimation from the wrapped Fried gradients. In Section 6, we provide several examples of the algorithm. Finally, in Section 7, the conclusions are presented.

2. NOTATION AND PRELIMINARIES

In this paper we deal with 2D signals $f(x,y)$, with x, y continuous, real variables representing a point in the 2D plane.

We define the 2D **Fourier transform** as

$$F(\kappa_x,\kappa_y) = \mathrm{FT}\{f(x,y)\} = \int_{-\infty}^{+\infty}\int_{-\infty}^{+\infty} f(x,y)e^{-j2\pi(\kappa_x x+\kappa_y y)}\mathrm{d}x\mathrm{d}y \tag{1}$$

with κ_x, κ_y having dimensions of 1/unit length.

When the 2D signal is sampled, we defined the 2D sampled sequence as

$$f[n_1,n_2] = f(n_1\Delta x, n_2\Delta y),$$

with integer indices n_1, n_2 and sample spacing Δx, Δy. For 2D discrete signals, we define the **z-Transform**

$$F(z_1,z_2) = Z\{f[n_1,n_2]\} = \sum_{n_1=-\infty}^{+\infty}\sum_{n_2=-\infty}^{+\infty} f[n_1,n_2]z_1^{-n_1}z_2^{-n_2}.$$

From the property (easy to show)

$$Z\{f[n_1+L_1,n_2+L_2]\} = z_1^{L_1}z_2^{L_2}Z\{f[n_1,n_2]\}$$

for any integer shift L_1 and L_2, we see that z_1 and z_2 are shift operators in the n_1 and n_2 directions, respectively.

By this interpretation we will make minimal use of the z-transform and rather use the shift operators as

$$f[n_1+L_1,n_2+L_2] = z_1^{L_1}z_2^{L_2}f[n_1,n_2].$$

Extension of the Fourier transform to the 2D sampled signal yields the 2D **discrete shift Fourier transform (DSFT)**, defined as

$$F(\boldsymbol{\omega}) = \sum_{n_1=-\infty}^{+\infty}\sum_{n_2=-\infty}^{+\infty} f[n_1,n_2]e^{-j(\omega_1 n_1+\omega_2 n_2)}.$$

The 2D digital frequency vector $\boldsymbol{\omega} = [\omega_1,\omega_2]$ has components

$$\omega_1 = 2\pi\kappa_x\Delta x, \qquad \omega_2 = 2\pi\kappa_y\Delta y,$$

and they are dimensionless expressed in *radians* or *radians per sample*. Also by the periodicity (2π in both dimensions) of the DSFT, the two frequency variables are usually constrained to the intervals

$$-\pi \le \omega_i < \pi$$

for $i = 1, 2$. All other values of ω are associated with aliased frequencies from the sampling process.

Also, since in this paper we will be addressing wrapped phase angles, call $\ell[n_1, n_2]$ any 2D sequence that assumes only integer values, i.e.,

$$\ell[n_1, n_2] \in \mathcal{Z}, \quad \forall\ n_1, n_2,$$

with $\mathcal{Z}$ denoting the set of signed integers.

3. VECTOR FIELD DECOMPOSITION

The Helmholtz decomposition states that a vector field in the 3D space is represented by a gradient component and a rotational component as

$$\psi = \nabla\phi + \nabla \times v, \tag{2}$$

where $\nabla = [\nabla_x, \nabla_y, \nabla_z]^T$ represents the gradient operator, $\phi(x, y, z) \in \mathbb{R}$ is the scalar potential, and $v(x, y, z) \in \mathbb{R}^3$ is the vector potential, with the outer product $\nabla\times$ defining the curl of the vector. In particular, in the case of a 2D vector field in the x, y plane,

$$\psi(x, y) = \begin{bmatrix} \psi_x(x, y) \\ \psi_y(x, y) \end{bmatrix}, \tag{3}$$

where we assume the component along the z axis to be identically zero, the scalar potential is $\phi(x, y)$, and the vector potential is along the z axis as $[0, 0, v(x, y)]^T$. This leads to a simple expression of the decomposition Eq. (3) in matrix form as

$$\begin{bmatrix} \psi_x(x, y) \\ \psi_y(x, y) \end{bmatrix} = \begin{bmatrix} \nabla_x & \nabla_y \\ \nabla_y & -\nabla_x \end{bmatrix} \begin{bmatrix} \phi(x, y) \\ v(x, y) \end{bmatrix}. \tag{4}$$

In the Fourier domain, Eq. (4) relates complex vectors as

$$\begin{bmatrix} \Psi_x(\boldsymbol{\kappa}) \\ \Psi_y(\boldsymbol{\kappa}) \end{bmatrix} = \begin{bmatrix} j2\pi\kappa_x & j2\pi\kappa_y \\ j2\pi\kappa_y & -j2\pi\kappa_x \end{bmatrix} \begin{bmatrix} \Phi(\boldsymbol{\kappa}) \\ V(\boldsymbol{\kappa}) \end{bmatrix}, \tag{5}$$

with $\Phi(\boldsymbol{\kappa})$ and $V(\boldsymbol{\kappa})$ the 2D Fourier transforms of $\phi(x, y)$ and $v(x, y)$, respectively, and $\boldsymbol{\kappa} = [\kappa_x, \kappa_y]$. This corresponds to the decomposition of the complex vector $\Psi(\boldsymbol{\kappa})$ in terms of the orthogonal reference frame defined by the two columns of the matrix in Eq. (5) above. Simple matrix inversion yields the two potentials (scalar and vector) computed as

$$((j2\pi\kappa_x)^2 + (j2\pi\kappa_y)^2) \begin{bmatrix} \Phi(\boldsymbol{\kappa}) \\ V(\boldsymbol{\kappa}) \end{bmatrix} = \begin{bmatrix} j2\pi\kappa_x & j2\pi\kappa_y \\ j2\pi\kappa y & -j2\pi\kappa_x \end{bmatrix} \begin{bmatrix} \Psi_x(\boldsymbol{\kappa}) \\ \Psi_y(\boldsymbol{\kappa}) \end{bmatrix}. \tag{6}$$

The problem of phase reconstruction is to recover the overall phase we call $\phi_0(x, y)$ from observed gradients $\psi(x, y)$. This is typical in adaptive optics [23] or interferometric synthetic aperture radars [24], where local phase differences are observed directly. When the vector field is irrotational, i.e., the curl component $v(x, y)$ is absent, the overall phase $\phi_0(x, y)$ is the same as the scalar gradient $\phi(x, y)$ since by definition,

$$\psi(x, y) = \nabla\phi(x, y).$$

Algorithms designed for this reconstruction are based on a matrix representation of phase differences [25–27] as

$$\mathrm{vec}(\psi[:, :]) = \boldsymbol{\Gamma}\,\mathrm{vec}(\phi[:, :]), \tag{7}$$

with vec(·) representing matrix-to-vector reshaping of sampled gradients ψ and potential ϕ, and Γ a matrix of appropriate dimensions with approximately twice the number of rows than columns. This yields an overdetermined set of equations solved by least squares as

$$\mathrm{vec}(\hat{\phi}[:, :]) = (\boldsymbol{\Gamma}^T\boldsymbol{\Gamma})^{-1}\boldsymbol{\Gamma}^T\,\mathrm{vec}(\psi[:, :]). \tag{8}$$

Although in the applications of interest, the observation vector $\psi(x, y)$ is made of phase gradients, the presence of singularities and the fact that all phase values are wrapped within the interval $[-\pi, \pi)$, makes the vector potential $v(x, y)$ to be nonzero. As a consequence, the phase $\hat{\phi}(x, y)$ to be estimated is not the same as the scalar potential $\phi(x, y)$. The substitution of Eq. (2) into Eq. (8) shows that the vector potential information is lost in the orthogonal frame. Therefore, the computation in Eq. (8) yields a least-squares approximation for the scalar potential and cannot account for the orthogonal component (the "hidden phase" in multiple references such as [3] and [4]) associated with the null space of the matrix $\boldsymbol{\Gamma}$ in Eq. (7).

A solution to this problem, proposed in this paper, is to use a different, nonorthogonal reference frame which will be shown in the next section to be well suited to the computation of phase data in the presence of phase wrapping and singularities such as branch points. In order to see this, we replace the representation in Eq. (4) with a nonorthogonal frame as follows:

$$\begin{bmatrix} \psi_x(x, y) \\ \psi_y(x, y) \end{bmatrix} = \begin{bmatrix} \nabla_x & 0 \\ \nabla_y & -\nabla_y \end{bmatrix} \begin{bmatrix} \phi_0(x, y) \\ \bar{c}(x, y) \end{bmatrix}, \tag{9}$$

or, equivalently,

$$\begin{bmatrix} \psi_x(x, y) \\ \psi_y(x, y) \end{bmatrix} = \begin{bmatrix} \nabla_x & \nabla_x \\ \nabla_y & 0 \end{bmatrix} \begin{bmatrix} \phi_1(x, y) \\ \bar{c}(x, y) \end{bmatrix}. \tag{10}$$

In this nonorthogonal frame, where the two basis vectors in the frequency domain are given by

$$e_1 = \begin{bmatrix} j2\pi\kappa_x \\ j2\pi\kappa_y \end{bmatrix}, \qquad e_2 = \begin{bmatrix} 0 \\ -j2\pi\kappa_y \end{bmatrix} \quad \text{or} \quad e_2 = \begin{bmatrix} j2\pi\kappa_x \\ 0 \end{bmatrix},$$

the two components $\phi_0(x, y)$ or $\phi_1(x, y)$ and $\bar{c}(x, y)$ are given by the following:

Lemma. Let $c(x, y)$ be the curl of the vector field $\psi(x, y)$, i.e.,

$$c(x,y) = \nabla_y \psi_x(x,y) - \nabla_x \psi_y(x,y), \tag{11}$$

and let $\phi(x,y)$, $v(x,y)$ be the scalar and vector potentials as in Eq. (4).

Also, define $\bar{c}(x,y)$ and $\bar{v}(x,y)$ in differential equation form such that

$$\begin{aligned} c(x,y) &\equiv \nabla_x \nabla_y \bar{c}(x,y), \\ v(x,y) &\equiv \nabla_x \nabla_y \bar{v}(x,y) \end{aligned} \tag{12}$$

with the boundary condition $w(x,y)$. The integral form of Eq. (12) is

$$\bar{c}(x,y) \equiv \int_0^y \int_0^x c(\lambda_1,\lambda_2)\mathrm{d}\lambda_1 \mathrm{d}\lambda_2 + w(x,y). \tag{13}$$

Then the vector field $\psi(x,y)$ can be expressed as in Eqs. (9) or (10) with

$$\begin{aligned} \phi_0(x,y) &= \phi(x,y) + \nabla_y^2 \bar{v}(x,y) + w_y(y), \\ \phi_1(x,y) &= \phi(x,y) - \nabla_x^2 \bar{v}(x,y) + w_x(x) \end{aligned} \tag{14}$$

with $w_x(x)$ and $w_y(y)$ depending on boundary conditions.

Proof. From the bottom equation in Eq. (6) and the definition of the curl $c(x,y)$ above, we obtain

$$(\nabla_x^2 + \nabla_y^2) v(x,y) = c(x,y).$$

Substitution of $v(x,y)$, $c(x,y)$ with $\bar{v}(x,y)$, $\bar{c}(x,y)$ as in Eq. (12) yields

$$(\nabla_x^2 + \nabla_y^2) \bar{v}(x,y) = \bar{c}(x,y) + w(x,y), \tag{15}$$

with $w(x,y)$ such that

$$\nabla_x \nabla_y w(x,y) = 0.$$

As shown in Appendix A, this implies that we can write $w(x,y)$ in the form

$$w(x,y) = w_x(x) - w_y(y).$$

Substituting $v(x,y)$ in Eq. (4) with $\nabla_x \nabla_y \bar{v}(x,y)$, we obtain

$$\begin{bmatrix} \psi_x \\ \psi_y \end{bmatrix} = \begin{bmatrix} \nabla_x \\ \nabla_y \end{bmatrix} \phi + \begin{bmatrix} \nabla_x \nabla_y^2 \bar{v} \\ \nabla_y \nabla_x^2 (-\bar{v}) \end{bmatrix}. \tag{16}$$

Combine Eq. (16) with Eq. (15) and we can rewrite it as

$$\begin{bmatrix} \psi_x \\ \psi_y \end{bmatrix} = \begin{bmatrix} \nabla_x \\ \nabla_y \end{bmatrix} (\phi + \nabla_y^2 \bar{v} + w_y) - \begin{bmatrix} 0 \\ \nabla_y \end{bmatrix} \bar{c}. \tag{17}$$

Call $\phi_0(x,y) = \phi(x,y) + \nabla_y^2 \bar{v}(x,y) + w_y(y)$ and the fact is proven. This relationship shows that $\phi_0(x,y)$ contains information from the scalar and vector potentials. The model in Eq. (10) follows immediately by adding the column vector $[\nabla_x, \nabla_y]^T \bar{c}(x,y)$ to both sides of Eq. (9), which yields

$$\phi_1(x,y) = \phi_0(x,y) - \bar{c}(x,y).$$

QED

The significance of this result is that, in certain cases, as addressed in the next section, the term $\phi_0(x,y)$ is the total phase and it can be computed from Eq. (9) as

$$\begin{bmatrix} \psi_x(x,y) \\ \psi_y(x,y) \end{bmatrix} + \begin{bmatrix} 0 \\ \nabla_y \bar{c}(x,y) \end{bmatrix} = \begin{bmatrix} \nabla_x \\ \nabla_y \end{bmatrix} \phi_0(x,y) \tag{18}$$

using standard techniques. From this result, a rotational field in $\psi(x,y)$ can be made irrotational by combining it with its own curl. In this case, $\phi_0(x,y)$, $\phi_1(x,y)$ or any combination thereof, becomes a possible scalar potential function. In the example below, where phase wrapping causes the phase gradient to become rotational, it is shown that the scalar potential $\phi_0(x,y)$ coincides with the actual phase $\theta(x,y)$, which is sensed by the wrapped gradients.

Based on the fact that any signal is equivalent to its own convolution with the impulse, as $c(x,y) = c(x,y) * *\delta(x)\delta(y)$, we can write

$$\begin{aligned} \bar{c}(x,y) &= c(x,y) * * u(x)u(y), \\ \nabla_x \bar{c}(x,y) &= c(x,y) * u(y), \\ \nabla_y \bar{c}(x,y) &= c(x,y) * u(x), \end{aligned} \tag{19}$$

with $u(\cdot)$ the unit step function and the "star" operations indicating 2D convolution with $u(x)u(y)$ and 1D convolutions with $u(x)$ and $u(y)$, respectively. For clarity, we note that the first line of Eq. (19) is equivalent to Eq. (13).

The following example illustrates the results in the Lemma presented above.

Example. Consider the phase

$$\theta(x,y) = \mathrm{phase}(x + jy)$$

with the phase wrapped to the interval $[0, 2\pi)$. Simple differentiation yields the *wrapped* gradient of θ and its Fourier transform, as computed in [4]:

$$\begin{aligned} \psi_x(x,y) &= -\frac{y}{x^2+y^2} \Leftrightarrow \Psi_x(\kappa_x,\kappa_y) = j\frac{\kappa_y}{\kappa_x^2+\kappa_y^2}, \\ \psi_y(x,y) &= \frac{x}{x^2+y^2} \Leftrightarrow \Psi_y(\kappa_x,\kappa_y) = -j\frac{\kappa_x}{\kappa_x^2+\kappa_y^2}. \end{aligned} \tag{20}$$

The actual *unwrapped* gradient of $\theta(x,y)$ has to take the discontinuity at $y = 0$, $x > 0$ into account as

$$\begin{bmatrix} \nabla_x \\ \nabla_y \end{bmatrix} \theta(x,y) = \begin{bmatrix} \psi_x(x,y) \\ \psi_y(x,y) \end{bmatrix} + \begin{bmatrix} 0 \\ 2\pi\delta(y)u(x) \end{bmatrix}. \tag{21}$$

From substituting Eq. (20) into Eq. (6), we can easily solve for the scalar potential $\Phi(\boldsymbol{\kappa})$, vector potential $V(\boldsymbol{\kappa})$, and the curl $C(\boldsymbol{\kappa})$ from Eq. (17) as

$$\begin{aligned} \Phi(\boldsymbol{\kappa}) &= 0, \\ V(\boldsymbol{\kappa}) &= \frac{1}{2\pi(\kappa_x^2+\kappa_y^2)}, \\ C(\boldsymbol{\kappa}) &= -2\pi. \end{aligned}$$

Now we can verify that Eq. (9) holds. We can substitute from Eq. (12) to solve

$$\nabla_x \nabla_y^2 \bar{v}(x,y) = \nabla_y v(x,y) = \text{IFT}\left\{\frac{j\kappa_y}{\kappa_x^2+\kappa_y^2}\right\}.$$

From Eq. (20), the right-hand side of the above equation is $\nabla_x \theta(x,y)$, and therefore

$$\nabla_y^2 \bar{v}(x,y) = \theta(x,y) + w_y(y)$$

with $w_y(y)$ accounting for boundary conditions. Substitution into Eq. (14) and using the fact that the scalar potential $\phi(x,y)$ is zero, we obtain

$$\phi_0(x,y) = \theta(x,y) + w_y(y). \tag{22}$$

This is the total phase we want to reconstruct, on the right-hand side of Eq. (18). Substituting for $\bar{c}$ on the left-hand side of Eq. (18), we obtain

$$\begin{bmatrix} \psi_x(x,y) \\ \psi_y(x,y) \end{bmatrix} + \begin{bmatrix} 0 \\ 2\pi u(x)\delta(y) \end{bmatrix} = \begin{bmatrix} \nabla_x \\ \nabla_y \end{bmatrix} \phi_0(x,y).$$

The left-hand side is $\nabla\theta(x,y)$ from Eq. (21). This implies

$$\theta(x,y) = \phi_0(x,y) + C,$$

where C is a constant. This is consistent with Eq. (22) and $w_y(y) = C$.

In the next section, where we addressed the sampled data implementation, we actually prove analytically that $\phi_0[n_1,n_2]$ and the phase sensed by the wrapped gradients differ by integer multiples of 2π, thus yielding the same wrapped values. In other words the "hidden phase" is included in ϕ_0, and therefore no "slope discrepancy" is in the gradients of ϕ_0.

4. FRIED GRADIENTS AND WRAPPED FRIED GRADIENTS

In the sampled data case, we extend the concepts introduced in the previous sections by defining the gradient operators on the basis of the Fried geometry [25].

To this extent, given the sampled phase $\phi_0[n_1,n_2] = \phi_0(n_1\Delta x, n_2\Delta y)$, we define the gradients in the two directions as

$$\begin{aligned}\psi_1[n_1,n_2] &= \frac{1}{2}(\phi_0[n_1+1,n_2+1] + \phi_0[n_1,n_2+1]) \\ &\quad - \frac{1}{2}(\phi_0[n_1+1,n_2] + \phi_0[n_1,n_2]), \\ \psi_2[n_1,n_2] &= \frac{1}{2}(\phi_0[n_1+1,n_2+1] + \phi_0[n_1+1,n_2]) \\ &\quad - \frac{1}{2}(\phi_0[n_1,n_2+1] + \phi_0[n_1,n_2]).\end{aligned}$$

Using the shift operators z_1, z_2, these can be written in a more compact form:

$$\begin{aligned}\psi_1[n_1,n_2] &= \frac{1}{2}(z_1+1)(z_2-1)\phi_0[n_1,n_2], \\ \psi_2[n_1,n_2] &= \frac{1}{2}(z_1-1)(z_2+1)\phi_0[n_1,n_2]\end{aligned}$$

from which we define the discrete gradient operators as

$$\begin{aligned}\nabla_1(z_1,z_2) &\equiv \frac{1}{2}(z_1+1)(z_2-1), \\ \nabla_2(z_1,z_2) &\equiv \frac{1}{2}(z_1-1)(z_2+1).\end{aligned} \tag{23}$$

Substituting $z_1 = e^{j\omega_1}$ and $z_2 = e^{j\omega_2}$ into Eq. (23), we obtain the discrete frequency response of the operators as

$$\begin{aligned}\nabla_1(\boldsymbol{\omega}) &= 2e^{-j\frac{\omega_1+\omega_2}{2}} \cos\left(\frac{\omega_1}{2}\right)\sin\left(\frac{\omega_2}{2}\right), \\ \nabla_2(\boldsymbol{\omega}) &= 2e^{-j\frac{\omega_1+\omega_2}{2}} \sin\left(\frac{\omega_1}{2}\right)\cos\left(\frac{\omega_2}{2}\right).\end{aligned}$$

It is easy to see that both $\nabla_1(\boldsymbol{\omega})$ and $\nabla_2(\boldsymbol{\omega})$ are zero when $\boldsymbol{\omega} = [0,0]$ ("piston" mode) and $\boldsymbol{\omega} = [\pi,\pi]$ ("waffle" mode). As a consequence,

$$\nabla x[\mathbf{n}] = 0 \Rightarrow x[\mathbf{n}] = C_0 + C_1(-1)^{n_1+n_2}$$

for some constants C_0, C_1 that depend on the boundary conditions with $\mathbf{n} = [n_1,n_2]$.

It is well known that Fried derivatives are good models for Shack–Hartmann sensors, which measure local phase gradients. However, Barchers demonstrated that the Fried geometry performance degrades in high scintillation when compared to Hudgin geometry [11]. When branch points causing phase wrapping are present, it is imperative to properly embed the wrapping operation within the Fried gradients computations. The development of the wrapped Fried gradient presented here is sufficient for reconstructing the high turbulence wavefront properly.

Figure 1 shows the block diagram approach of the Fried geometry. In (a), on the left, the standard Fried gradients are shown in terms of transfer functions in z_1 and z_2. The first blocks (z_1-1) and (z_2-1) provide for phase differences in the vertical and horizontal directions, while the second blocks $(z_2+1)/2$ and $(z_1+1)/2$ provide simple averaging (half the sum) in the opposite directions (horizontal and vertical).

When phase wrapping is present, the first block, which models phase difference measurements, has to be augmented with the phase wrapping operation $\mathcal{W}$, defined as

$$\theta[\mathbf{n}] = \mathcal{W}(\alpha[\mathbf{n}]) \equiv \alpha[\mathbf{n}] + 2\pi\ell[\mathbf{n}]$$

with $\ell[\mathbf{n}]$ an appropriate integer sequence so that $-\pi \le \theta[\mathbf{n}] < \pi$ for all $\mathbf{n}$. This guarantees that phase differences multiples of 2π are not sensed.

Call $\nabla\mathcal{W}$ the wrapped Fried derivative gradient in Fig. 1(b) and $\psi[\mathbf{n}]$, the sensed wrapped gradients, as

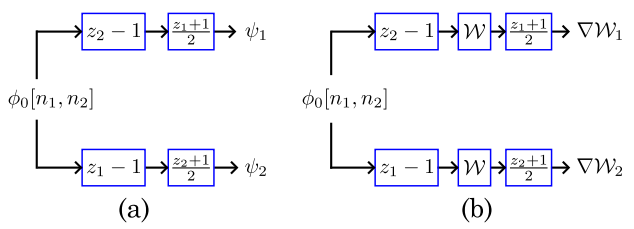

Fig. 1. Block diagram form (a) the traditional Fried gradient and (b) the wrapped Fried gradient.

$$\psi[n_1,n_2]=\begin{bmatrix}\nabla\mathcal{W}_1\\ \nabla\mathcal{W}_2\end{bmatrix}\phi_0[n_1,n_2].$$

From the definition of the wrapping operator $\mathcal{W}$ and the factor $1/2$ in the averaging second block we can relate ∇ and $\nabla\mathcal{W}$ as

$$\nabla\mathcal{W}\phi_0[\mathbf{n}]=\nabla\phi_0[\mathbf{n}]+\pi\ell[\mathbf{n}] \tag{24}$$

with $\ell[\mathbf{n}]$ assuming integer values only.

This will be the basis of the phase estimation presented in the next section.

5. LEAST-SQUARES PHASE ESTIMATION FROM WRAPPED FRIED GRADIENTS

Along the same lines as in the previous section, the vector field ψ can be represented in terms of scalar and potential functions ϕ and v as

$$\begin{bmatrix}\psi_1[n_1,n_2]\\ \psi_2[n_1,n_2]\end{bmatrix}=\begin{bmatrix}\nabla_1 & \nabla_2\\ \nabla_2 & -\nabla_1\end{bmatrix}\begin{bmatrix}\phi[n_1,n_2]\\ v[n_1,n_2]\end{bmatrix}.$$

Same as for the continuous case in the previous section, in the frequency domain this just becomes a matrix–vector operation:

$$\begin{bmatrix}\Psi_1(\boldsymbol{\omega})\\ \Psi_2(\boldsymbol{\omega})\end{bmatrix}=e^{-j\frac{\omega_1+\omega_2}{2}}\begin{bmatrix}c_1s_2 & s_1c_2\\ s_1c_2 & -c_1s_2\end{bmatrix}\begin{bmatrix}\Phi(\boldsymbol{\omega})\\ V(\boldsymbol{\omega})\end{bmatrix}$$

with $c_i=\cos(\omega_i/2)$ and $s_i=\sin(\omega_i/2)$ for $i=1,2$. We can easily verify that the two columns of the matrix represent two orthogonal vectors.

The result of the previous section can then be extended to the sampled data case by defining the curl of the vector field as

$$c[n_1,n_2]\equiv\nabla_2\psi_1[n_1,n_2]-\nabla_1\psi_2[n_1,n_2],$$

with ∇_1, ∇_2 the standard unwrapped Fried derivatives. Then the vector field ψ can be expressed as

$$\begin{bmatrix}\psi_1[n_1,n_2]\\ \psi_2[n_1,n_2]\end{bmatrix}=\begin{bmatrix}\nabla_1 & 0\\ \nabla_2 & -\nabla_2\end{bmatrix}\begin{bmatrix}\phi_0[n_1,n_2]\\ \bar{c}[n_1,n_2]\end{bmatrix}$$

with $\bar{c}$ defined as

$$c[n_1,n_2]\equiv\nabla_1\nabla_2\bar{c}[n_1,n_2]. \tag{25}$$

In order to obtain an expression for $\bar{c}$, first notice that any signal can be represented in convolution (double convolution in the 2D case) form

$$c[n_1,n_2]=c[n_1,n_2]**\delta[n_1]\delta[n_2]$$

with $\delta[n]$ the discrete impulse, being $\delta[0]=1$ and $\delta[n]=0$ for all $n\neq 0$. In Eq. (25), the product of the two operators can be expressed as

$$\begin{aligned}\nabla_1(z)\nabla_2(z)&=\frac{1}{4}(z_1-1)(z_1+1)(z_2-1)(z_2+1)\\&=\frac{1}{4}(z_1^2-1)(z_2^2-1).\end{aligned}$$

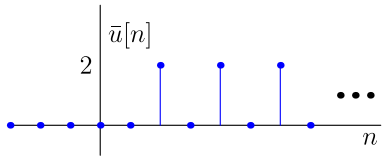

Fig. 2. Function $\bar{u}[\mathbf{n}]$ is used to create $\bar{c}[\mathbf{n}]$ from $c[\mathbf{n}]$.

Now if we define the sequence

$$\bar{u}[n]\equiv(1+(-1)^n)u[n-2],$$

plotted in Fig. 2, we can verify that $\bar{u}[n+2]-\bar{u}[n]=2\delta[n]$, and therefore

$$\delta[n_1]\delta[n_2]=\nabla_1(z)\nabla_2(z)\bar{u}[n_1]\bar{u}[n_2],$$

so that $\bar{c}$ can be written as

$$\bar{c}[n_1,n_2]=c[n_1,n_2]**\bar{u}[n_1]\bar{u}[n_2].$$

With these premises we can state the main result of this research.

Main Result. Let $\psi[n_1,n_2]$ be the vector field of the wrapped Fried gradient of the phase $\phi_0[n_1,n_2]$, defined as

$$\begin{bmatrix}\psi_1[\mathbf{n}]\\ \psi_2[\mathbf{n}]\end{bmatrix}=\begin{bmatrix}\nabla\mathcal{W}_1\\ \nabla\mathcal{W}_2\end{bmatrix}\phi_0[\mathbf{n}].$$

Also let its curl, $c[\mathbf{n}]$, be such that

$$c[\mathbf{n}]=\pi\ell[\mathbf{n}],$$

i.e., it assumes values only integer multiples of π.

Let be $\hat{\phi}[\mathbf{n}]$ such that

$$\begin{bmatrix}\psi_1[\mathbf{n}]\\ \psi_2[\mathbf{n}]\end{bmatrix}+\begin{bmatrix}0\\ c[\mathbf{n}]**q[\mathbf{n}]\end{bmatrix}=\begin{bmatrix}\nabla_1\\ \nabla_2\end{bmatrix}\hat{\phi}[\mathbf{n}], \tag{26}$$

with $**$ denoting 2D convolution, and $q[\mathbf{n}]$ defined as

$$q[n_1,n_2]\equiv\frac{1}{2}(z_1-1)(z_2+1)\bar{u}[n_1,n_2].$$

Then there exist constants C_0, C_1 for which

$$\phi_0[\mathbf{n}]=\hat{\phi}[\mathbf{n}]+C_0+C_1(-1)^{n_1+n_2}+2\pi\ell[\mathbf{n}], \tag{27}$$

with the rightmost term a sequence assuming only integer multiples of 2π.

Proof. By exactly the same arguments as in the previous section, Eq. (26) holds for some $\hat{\phi}[\mathbf{n}]$. What we need to show is that the estimated phase $\hat{\phi}[\mathbf{n}]$ and the original phase $\phi_0[\mathbf{n}]$ are the same apart from integer multiples of 2π, a piston mode C_0 and a "waffle" mode $C_1(-1)^{n_1+n_2}$.

The argument is based on the fact that the curl sequence $c[n_1,n_2]$ assumes values that are all integer multiples of π. Also it is a simple exercise to verify that the sequence $q[\mathbf{n}]=0,\pm 2$ for all n. As a consequence, for all $\mathbf{n}$,

$$c[\mathbf{n}]**q[\mathbf{n}]=2\pi\ell[\mathbf{n}],$$

where, again $\ell[\mathbf{n}]$ denotes a sequence of integer values. Recall that the relation between Fried and wrapped Fried gradients in Eq. (24) and the observed wrapped phase gradient $\psi[\mathbf{n}]$. Then by substituting into Eq. (26) we obtain that the sequence

$$\begin{bmatrix} \nabla_1 \\ \nabla_2 \end{bmatrix}(\phi_0[\mathbf{n}] - \hat{\phi}[\mathbf{n}]) = \pi \begin{bmatrix} \ell_1[\mathbf{n}] \\ \ell_2[\mathbf{n}] \end{bmatrix}, \tag{28}$$

i.e., it assumes values that are integer multiples of π for all $\mathbf{n}$. Since for any sequence

$$\ell[\mathbf{n}] = \ell[\mathbf{n}] * *\delta[n_1]\delta[n_2]$$

and

$$\begin{aligned}\delta[n_1]\delta[n_2] &= \nabla_1(2(-1)^{n_1-1}u[n_1-1]u[n_2-1]) \\ &= \nabla_2(2(-1)^{n_2-1}u[n_1-1]u[n_2-1]),\end{aligned}$$

we have that

$$\ell[\mathbf{n}] = 2\nabla_1\ell[\mathbf{n}]\ell[\mathbf{n}] = 2\nabla_2\ell[\mathbf{n}]. \tag{29}$$

In other words, a sequence of integers is the Fried derivative of a sequence of even integers. Finally, combine Eqs. (28) and (29) to obtain

$$\nabla(\phi_0[\mathbf{n}] - \hat{\phi}[\mathbf{n}] + 2\pi\ell[\mathbf{n}]) = 0,$$

which proves the result. QED

Estimation of $\phi_0[\mathbf{n}]$ based on sensed Fried gradients $\psi[\mathbf{n}]$ is then carried out by computing $\hat{\phi}[\mathbf{n}]$ from Eq. (26), using either standard least squares or (as is shown in the next section) the multiresolution algorithm presented by the authors in [28].

Then, from the result in Eq. (27),

$$\phi_0[\mathbf{n}] = \mathcal{W}(\hat{\phi}[\mathbf{n}] + C_0) \tag{30}$$

with C_0 a constant determined by a reference value. The "waffle" term is usually neglected since the data is assumed not to contain this term.

The algorithm for Fried geometry can be summarized as a procedural list:

1. Collect the sensor measurements $\psi_1[n_1, n_2]$ and $\psi_2[n_1, n_2]$.
2. Compute the curl

$$c[n_1, n_2] = \nabla_2\psi_1[n_1, n_2] - \nabla_1\psi_2[n_1, n_2].$$

3. Compute the quantity

$$\nabla_2\bar{c}[n_1, n_2] = c[n_1, n_2] * *q[n_1, n_2].$$

4. Modify the measurement

$$\psi_{2,\text{new}}[n_1, n_2] = \psi_2[n_1, n_2] + \nabla_2\bar{c}[n_1, n_2].$$

5. Use $\psi_1[n_1, n_2]$ and $\psi_{2,\text{new}}[n_1, n_2]$ in the standard least-squares reconstructor to solve for $\hat{\phi}[n_1, n_2]$:

$$\begin{bmatrix} \psi_1[n_1, n_2] \\ \psi_{2,\text{new}}[n_1, n_2] \end{bmatrix} = \begin{bmatrix} \nabla_1 \\ \nabla_2 \end{bmatrix}\hat{\phi}[n_1, n_2].$$

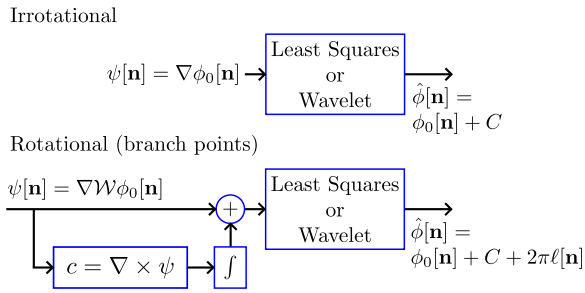

Fig. 3. Block diagram comparison of the traditional least-squares approach to the new form that is capable of handling branch points. When the curl is equal to zero, the output is exactly the same for both forms.

The comparison of this algorithm with the traditional approach is given in Fig. 3.

6. APPLICATION TO PHASE ESTIMATION

The algorithm presented in Section 5 has been applied to a number of phase signals both geometric and simulated wavefront phase functions.

In the following examples when noise is present, the Gaussian white noise is added to the phase difference measurement quantities as

$$\begin{bmatrix} \psi_{x,\text{noisy}}[n_1, n_2] \\ \psi_{y,\text{noisy}}[n_1, n_2] \end{bmatrix} = \begin{bmatrix} \psi_x[n_1, n_2] \\ \psi_y[n_1, n_2] \end{bmatrix} + \begin{bmatrix} \alpha n_x[n_1, n_2] \\ \alpha n_y[n_1, n_2] \end{bmatrix},$$

where α is chosen to ensure the desired SNR for simulation. Unless stated otherwise, amplitude is not used in the reconstruction and no noise added to the amplitude.

In addition, we provide a comparison with the proprietary SPhase algorithm in AOTools/WaveProp, developed by the Optical Sciences Company [29,30]. SPhase uses amplitude and phase information for wavefront reconstruction and its goal is to place the branch cuts in areas of low intensity for a continuous deformable mirror. SPhase also performs phase unwrapping. Thus, the goals of SPhase are different than the algorithm presented here.

A. Example 1: Geometric Signal

Let $s = x + jy$ and define $\phi_0[\mathbf{n}]$ as samples of the phase

$$\phi(x, y) = \text{phase}(s)$$

with sampling intervals $\delta_x = \delta_y = 0.01$, the number of data points $N = 256 \times 256$, and a shift by $\delta_x/2$ and $\delta_y/2$ so that the singular point $x = y = 0$ is not in the sampling grid.

Figure 4 shows the 3D plot of the wrapped phase $\mathcal{W}\phi_0[\mathbf{n}]$ and Fig. 5 shows the wrapped estimated phase $\mathcal{W}\hat{\phi}[\mathbf{n}]$ and demonstrates perfect reconstruction. The significance of this is observable from Figs. 6 and 7, where the large discontinuity is not apparent. This is the importance of the wrapped Fried gradient model, otherwise the ridge would be in the gradient data that is the input to the algorithm.

In this particular example, because the discontinuity is along the same dimension as our nonorthogonal correction, the result is exactly the same as the input. If the input had a discontinuity at a different angle relative to the origin (which would still result in the same wrapped measurements), the

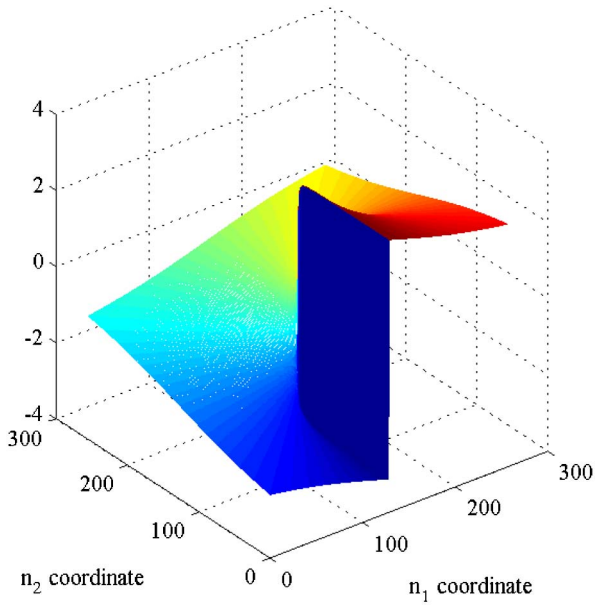

Fig. 4. Original $\phi[\mathbf{n}]$ phase data for example 1.

resulting output would still be the same as the one shown in Fig. 5.

B. Example 2: Geometric Signal

Similarly, Fig. 8 shows the samples of the phase for the function

$$\phi(x,y) = \text{phase}\left(\frac{(s-b_1)(s-b_2)}{(s-a)}\right) \tag{31}$$

with $b_1 = 0.5150 - j0.26$, $b_2 = 0.0050 + j0.26$, and $a = 0.005 + j0.005$. Two estimates are shown: without noise in Fig. 9 and with noise added to the observations (with 40 dB SNR) in Fig. 10.

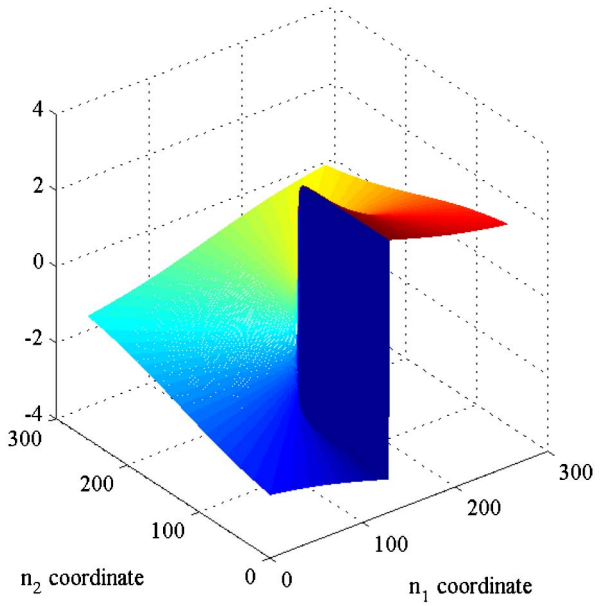

Fig. 5. Reconstructed $\mathcal{W}\hat{\phi}[\mathbf{n}]$ phase data for example 1.

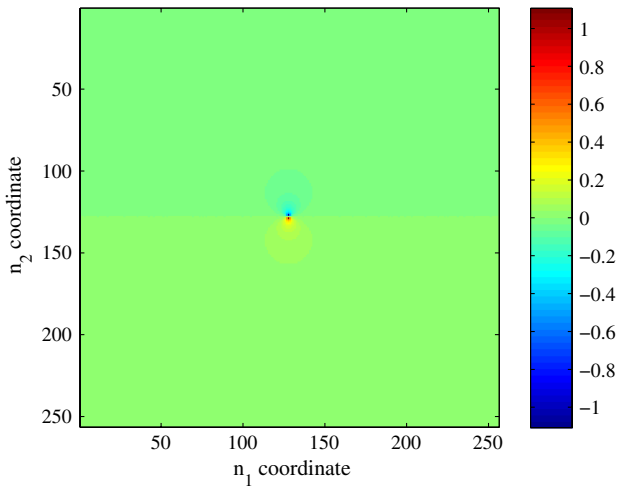

Fig. 6. Wrapped gradient $\psi_1[\mathbf{n}]$ data for example 1. The large discontinuity seen in Fig. 4 is not apparent in the wrapped measured gradient.

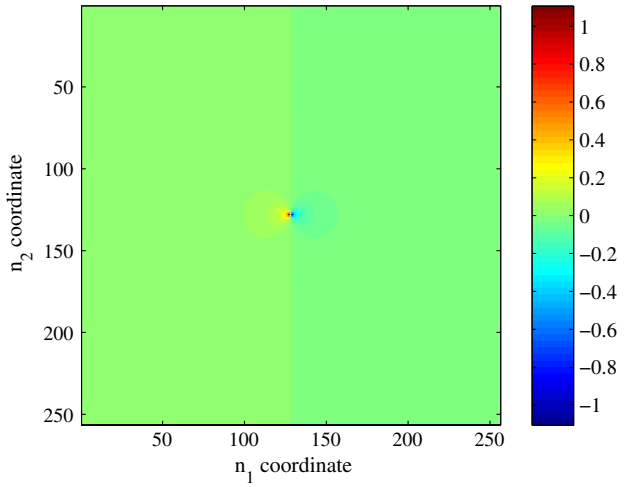

Fig. 7. Wrapped gradient $\psi_2[\mathbf{n}]$ data for example 1. The large discontinuity seen in Fig. 4 is not apparent in the wrapped measured gradient. The correction term proposed in this paper will be added to $\psi_2[\mathbf{n}]$ to create the large discontinuity.

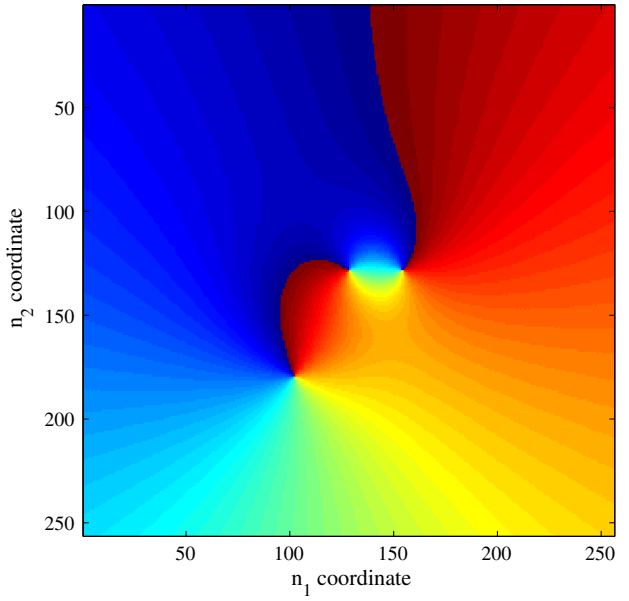

Fig. 8. Original $\phi[\mathbf{n}]$ plotted for example 2.

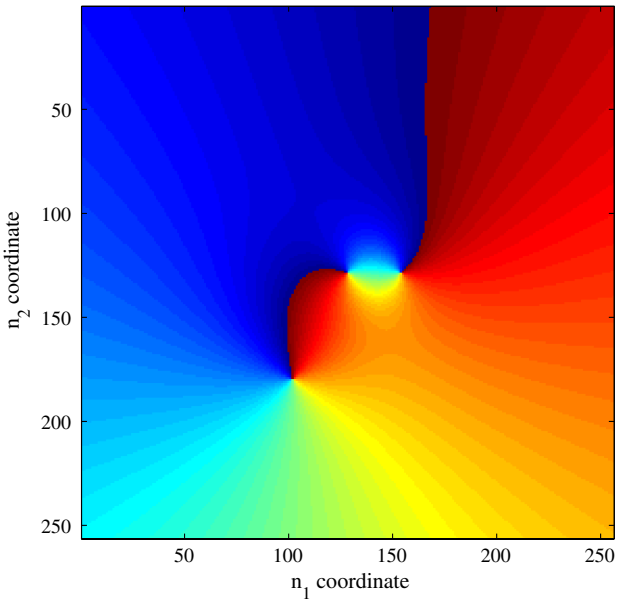

Fig. 9. Estimated phase $\mathcal{W}\hat{\phi}[\mathbf{n}]$ plotted for example 2.

Comparison of Figs. 8 and 9 along the top center shows two different boundaries of maximum (red) and minimum phase (blue). In this example, we show that C_0 from Eq. (30) is set to a constant that causes a slightly different wrapping than Fig. 8. The gradient measurements are the same and we show that the discontinuity can be positioned.

With this example, we are able to know the amplitude and phase. If we run SPhase with the phase, but set the uniform amplitude to be unity, SPhase chooses a simple branch cut scheme of connecting the two closest branch points to one another, and the third (closer to the bottom) branch point straight to the bottom edge. Our algorithm connects the lower branch point to the right edge (due to the nonorthogonal basis). Wrapping the phase for either result has the same output.

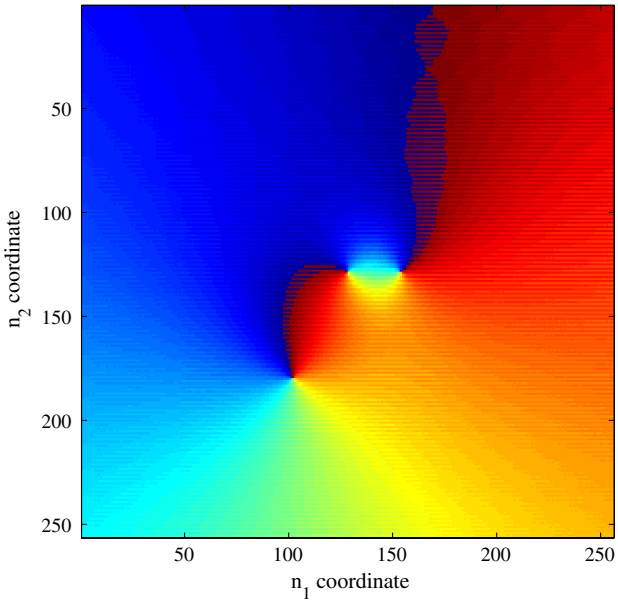

Fig. 10. Estimated phase $\mathcal{W}\hat{\phi}[\mathbf{n}]$ with 40 dB SNR for example 2. Pixels with values close to $-\pi$ or π may wrap due to the noise.

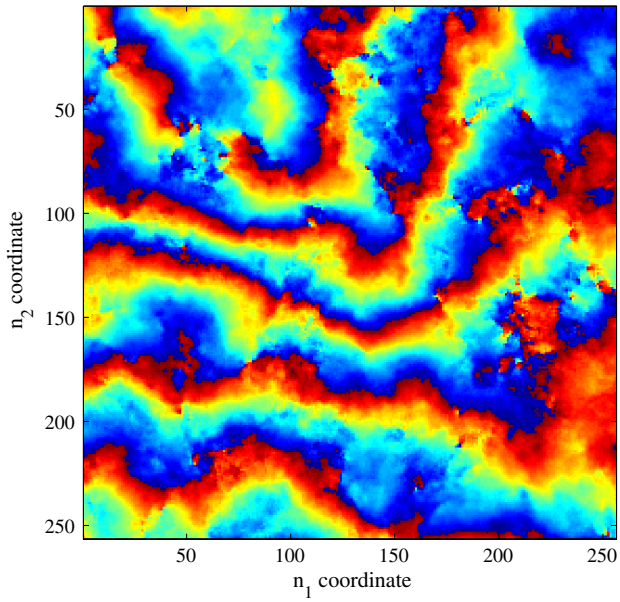

Fig. 11. High turbulence wavefront phase $\phi[\mathbf{n}]$ created using WaveProp for example 3.

Using both the amplitude and phase information from Eq. (31), SPhase creates a slightly more complicated branch cut between the upper two branch points that takes advantage of the lower intensity path between these singularities.

C. Example 3: High Turbulence Phase Signal

WaveProp was used to generate the algorithm input data for this example. We tried the algorithm under a variety of operation conditions, but only present the highest turbulence results here as other cases also were successful. WaveProp simulated a 1.0 m diameter circular aperture in a 2048×2048 E-field grid. The simulation used $\lambda = 1$ μm through a 4 km horizontal path. The atmospheric effects were assumed to be a constant turbulence through five phase screens. The C_n^2 value is 7×10^{-15} with a calculated Rytov number of 0.3051.

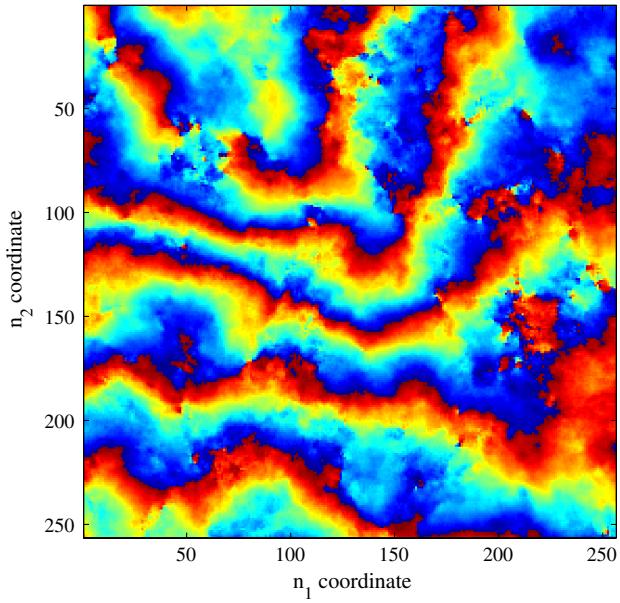

Fig. 12. Estimated wavefront $\mathcal{W}\hat{\phi}[\mathbf{n}]$ reconstructed for example 3.

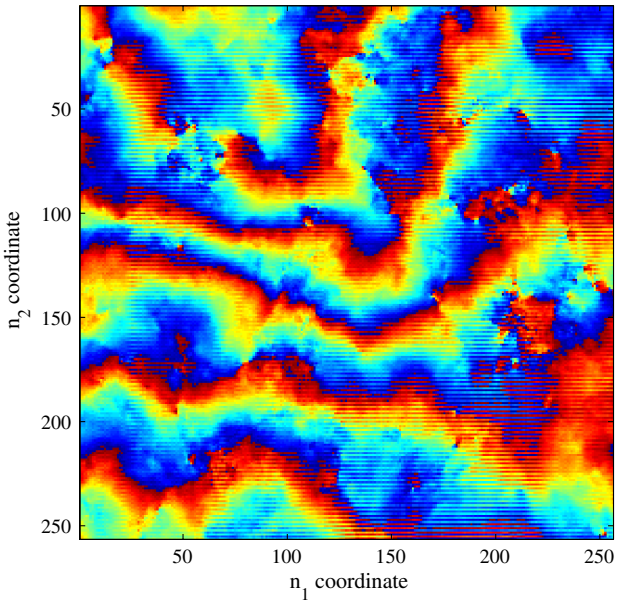

Fig. 13. Estimated wavefront $\mathcal{W}\hat{\phi}[\mathbf{n}]$ reconstructed with 40 dB SNR.

The phase signal is shown in Fig. 11, with estimates in Fig. 12 (no noise) and Fig. 13 (noise with 40 dB SNR). For the noiseless case, Fig. 14 shows the location of the detected branch points, while Fig. 15 shows the branch points of the original phase as determined by WaveProp.

SPhase only works on this example when the correct (original) amplitude is also supplied to its input. Setting a constant amplitude results in a signal of little interest (even the wrapped output did not match the original data). The wrapped output of SPhase (using the WaveProp amplitude) is identical to the output of our algorithm. Thus, we can say that the amplitude information is important in the SPhase algorithm, whereas the amplitude is not used by our algorithm proposed here.

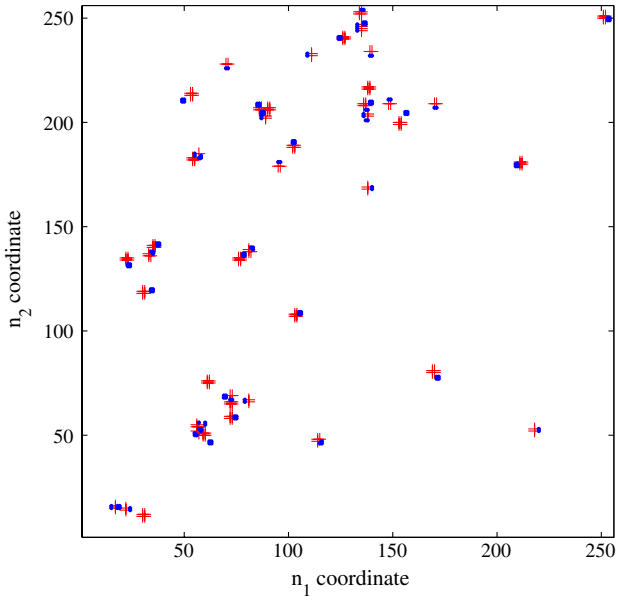

Fig. 14. Detected branch points for example 3 with no noise. Positive branch points are indicated with a red plus while negative branch points are indicated with a blue dot. Because the Fried geometry averages neighboring values, the locations on this plot are quadrupled compared to Fig. 15.

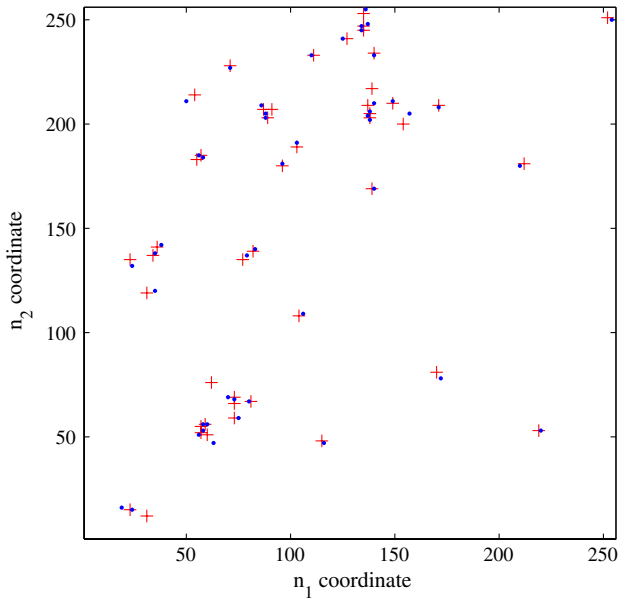

Fig. 15. Known branch points for example 3 with no noise. Locations were determined by WaveProp. Positive branch points are indicated with a red plus while negative branch points are indicated with a blue dot.

D. Example 4: Double Spiral

Our last example is the double-spiral shear from [7]. Although this dataset, shown in Fig. 16, is used to test unwrapping, we decided to include it here. Ghiglia states that this example has failed in unwrapping when there is noise on the measurements for all unwrapping algorithms covered by their book. The actual spiral data has one arm ascending (with a positive n_1 gradient) and the other spiral arm descending with a negative n_1 gradient of the same magnitude.

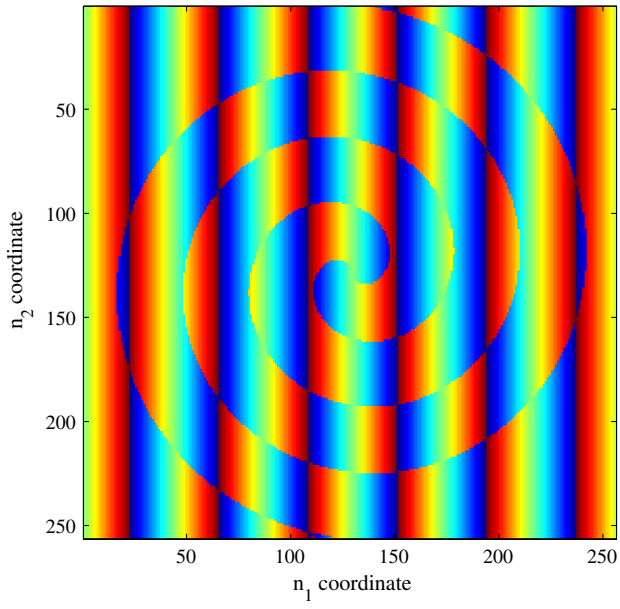

Fig. 16. Spiral dataset $\phi[\mathbf{n}]$ from [7]. This dataset is known to be difficult to process correctly.

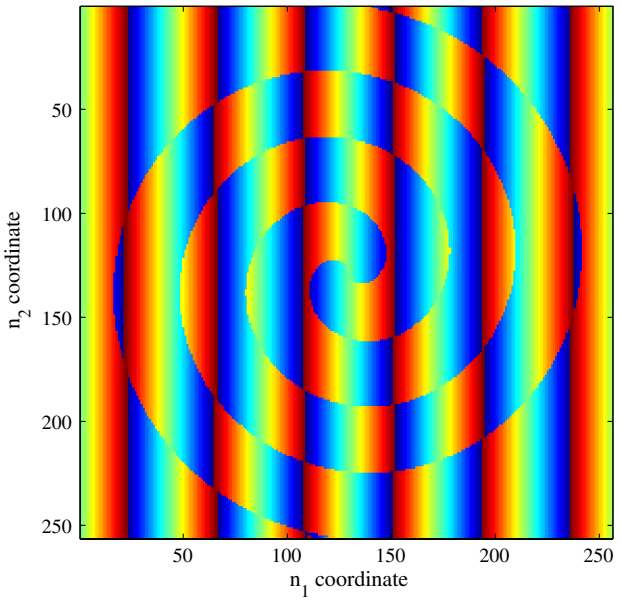

Fig. 17. Estimated phase $\mathcal{W}\hat{\phi}[\mathbf{n}]$ reconstructed for the spiral dataset.

Our algorithm results in Fig. 17 for no noise, and in Fig. 18 for 40 dB SNR. In the case of noise, the noise can potentially cause the phase value to wrap and the horizontal bar pattern can form. However, in the no noise case, the reconstruction is exact. The determined branch point locations match Figure 3.10 in [7].

Since SPhase also includes unwrapping, it has difficulty on this dataset. While its output does show the double-spiral pattern, the spiral arms are flat areas. The boundary pixels between the spiral arms often do not fully resolve correctly and have discontinuities. The wrapped output of SPhase is not a good match to the original surface. One spiral arm takes on zero value for all pixels, and the other spiral arm has areas that are close to $\pm\pi$. The boundary pixels of the spirals in the wrapped output also have discontinuities.

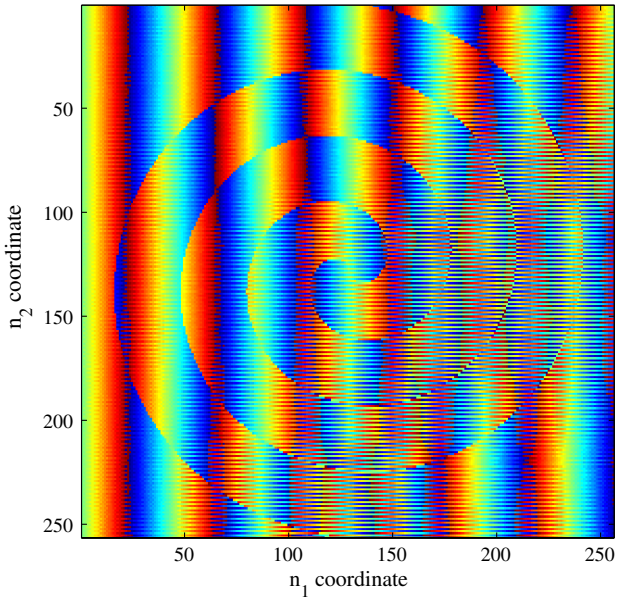

Fig. 18. Estimated phase $\mathcal{W}\hat{\phi}[\mathbf{n}]$ reconstructed for spiral dataset with 40 dB SNR.

7. CONCLUSION

In this research, we addressed the problem of estimating a phase signal based on observation of wrapped local variations. This approach is based on a particular representation of the vector field in terms of a nonorthogonal basis, which seems to be better suited than the standard orthogonal basis associated with scalar and potential field.

It is shown that, correcting the observed gradient with a filtered curl, the overall phase (including what has been called the "hidden phase") is estimated by standard least-squares solver. A number of computer simulations support what has been stated based on mathematical analysis. A comparison with SPhase shows that our algorithm results in the same wrapped phase measurements, which is expected since the algorithms output different phase functions of the ensemble of wavefront surfaces that have the same gradient measurements. The examples show that the wrapped ϕ_0 is equal to the wrapped total phase.

This approach is able to efficiently determine a wavefront surface that is a member of the ensemble of wavefronts that all have the same gradient measurements. The approach is as computationally efficient as the least-squares or equivalent reconstructor chosen. The approach does not unwrap the phase, as we leave that as a follow-on step to the output of our algorithm presented here.

APPENDIX A:

Let $w(x, y)$

$$\nabla_x \nabla_y w(x, y) = 0$$

for all x, y real. Then $w(x, y)$ can be written as

$$w(x, y) = a(x) + b(y).$$

To show this, define

$$g(x, y) = \nabla_x w(x, y). \tag{A1}$$

Then $\nabla_y g(x, y) = 0$ and therefore,

$$g(x, y) = g(x, 0),$$

i.e., independent of y. Substitute in Eq. (A1) to obtain

$$w(x, y) = w(0, y) + \int_0^x g(\lambda, 0)\mathrm{d}\lambda,$$

which shows the result.

ACKNOWLEDGMENTS

This research was performed with the Adaptive Optics Center of Excellence in National Security located at the Naval Postgraduate School. Gratitude is also expressed to the anonymous reviewer, whose comments improved the quality of the paper. The authors also appreciate the helpful discussions with David L. Fried, Lew De Sandre, Terry Brennan, and Sergio Restaino. The views expressed in this document are those of the author and do not reflect the official policy or position of the Department of Defense or the U.S. Government.

REFERENCES

1. J. F. Nye and M. V. Berry, "Dislocations in wave trains," Proc. R. Soc. A **336**, 165–190 (1974).
2. D. L. Fried and J. L. Vaughn, "Branch cuts in the phase function," Appl. Opt. **31**, 2865–2882 (1992).
3. D. L. Fried, "Branch point problem in adaptive optics," J. Opt. Soc. Am. A **15**, 2759–2768 (1998).
4. G. Tyler, "Reconstruction and assessment of the least-squares and slope discrepancy components of the phase," J. Opt. Soc. Am. A **17**, 1828–1839 (2000).
5. D. L. Fried, "Adaptive optics wave function reconstruction and phase unwrapping when branch points are present," Opt. Commun. **200**, 43–72 (2001).
6. R. Goldstein, H. A. Zebker, and C. L. Werner, "Satellite radar interferometry: two-dimensional phase unwrapping," Radio Sci. **23**, 713–720 (1988).
7. D. C. Ghiglia and M. D. Pritt, *Two-Dimensional Phase Unwrapping: Theory, Algorithms, and Software* (Wiley, 1998).
8. T. M. Venema and J. D. Schmidt, "Optical phase unwrapping in the presence of branch points," Opt. Express **16**, 6985–6998 (2008).
9. C. Pellizzari, "Phase unwrapping in the presence of strong turbulence," in *IEEE Aerospace Conference* (IEEE, 2010).
10. C. Pellizzari and J. D. Schmidt, "Phase unwrapping in the presence of strong turbulence," *IEEE Aerospace Conference* (2010), pp. 1–10.
11. J. D. Barchers, D. L. Fried, and D. J. Link, "Evaluation of the performance of Hartmann sensors in strong scintillation," Appl. Opt. **41**, 1012–1021 (2002).
12. J. D. Barchers, D. L. Fried, D. J. Link, G. A. Tyler, W. Moretti, T. J. Brennan, and R. Q. Fugate, "The performance of wavefront sensors in strong scintillation," Proc. SPIE **4839**, 217–227 (2003).
13. E.-O. Le Bigot and W. J. Wild, "Theory of branch-point detection and its implementation," J. Opt. Soc. Am. A **16**, 1724–1729 (1999).
14. K. Murphy, R. Mackey, and C. Dainty, "Branch point detection and correction using the branch point potential method," Proc. SPIE **6951**, 695105 (2008).
15. V. E. Zetterlind III and E. P. Magee, "Performance of various branch point tolerant phase reconstructors with finite time delays and measurement noise," Proc. SPIE **4632**, 85–94 (2002).
16. D. J. Sanchez and D. W. Oesch, "The aggregate behavior of branch points: the creation and evolution of branch points," Proc. SPIE **7466**, 746605 (2009).
17. D. W. Oesch, D. J. Sanchez, C. M. Tewksbury-Christle, and P. R. Kelly, "The aggregate behavior of branch points: altitude and strength of atmospheric turbulence layers," Proc. SPIE **7816**, 781605 (2010).
18. D. J. Sanchez, D. W. Oesch, and P. R. Kelly, "The aggregate behavior of branch points: theoretical calculation of branch point velocity," Proc. SPIE **8380**, 83800P (2012).
19. D. W. Oesch, D. J. Sanchez, and C. M. Tewksbury-Christle, "Aggregate behavior of branch points–persistent pairs," Opt. Express **20**, 1046–1059 (2012).
20. D. W. Oesch, D. J. Sanchez, and C. L. Matson, "The aggregate behavior of branch points-measuring the number and velocity of atmospheric turbulence layers," Opt. Express **18**, 22377–22392 (2010).
21. D. J. Sanchez and D. W. Oesch, "Localization of angular momentum in optical waves propagating through turbulence," Opt. Express **19**, 25388–25396 (2011).
22. D. J. Sanchez and D. W. Oesch, "Orbital angular momentum in optical waves propagating through distributed turbulence," Opt. Express **19**, 24596–24608 (2011).
23. F. Roddier, *Adaptive Optics in Astronomy* (Cambridge University, 1999).
24. R. C. Olsen, *Remote Sensing from Air and Space* (SPIE, 2007).
25. D. L. Fried, "Least-square fitting a wave-front distortion estimate to an array of phase-difference measurements," J. Opt. Soc. Am. **67**, 370–375 (1977).
26. R. H. Hudgin, "Wave-front reconstruction for compensated imaging," J. Opt. Soc. Am. **67**, 375–378 (1977).
27. L. A. Poyneer, D. T. Gavel, and J. M. Brase, "Fast wave-front reconstruction in large adaptive optics systems with use of the Fourier transform," J. Opt. Soc. Am. A **19**, 2100–2111 (2002).
28. T. W. Axtell and R. Cristi, "Generalized orthogonal wavelet phase reconstruction," J. Opt. Soc. Am. A **30**, 859–870 (2013).
29. T. J. Brennan and P. H. Roberts, *AOTools: the Adaptive Optics Toolbox for Use with MATLAB*, Optical Sciences Company User's Guide 1.4a (Optical Sciences Company, 2010).
30. T. J. Brennan, P. H. Roberts, and D. C. Mann, *WaveProp: a Wave Optics Simulation System for Use with MATLAB*, Optical Sciences Company User's Guide 1.3 (Optical Sciences Company, 2010).